THE JOURNAL OF PHYSICAL CHEMISTRY B

pubs.acs.org/JPCB Article

Molecular Dynamics Simulations Based on Newly Developed Force Field Parameters for Cu^{2+} Spin Labels Provide Insights into Double-Histidine-Based Double Electron−Electron Resonance

Xiaowei Bogetti, Shreya Ghosh, Austin Gamble Jarvi, Junmei Wang,* and Sunil Saxena*

Cite This: *J. Phys. Chem. B* 2020, 124, 2788−2797 Read Online

ACCESS | Metrics & More | Article Recommendations | Supporting Information

ABSTRACT: Electron paramagnetic resonance (EPR) in combination with the recently developed double-histidine (dHis)-based Cu^{2+} spin labeling has provided valuable insights into protein structure and conformational dynamics. To relate sparse distance constraints measured by EPR to protein fluctuations in solution, modeling techniques are needed. In this work, we have developed force field parameters for Cu^{2+}−nitrilotriacetic and Cu^{2+}−iminodiacetic acid spin labels. We employed molecular dynamics (MD) simulations to capture the atomic-level details of dHis-labeled protein fluctuations. The interspin distances extracted from 200 ns MD trajectories show good agreement with the experimental results. The MD simulations also illustrate the dramatic rigidity of the Cu^{2+} labels compared to the standard nitroxide spin label. Further, the relative orientations between spin-labeled sites were measured to provide insight into the use of double electron−electron resonance (DEER) methods for such labels. The relative mean angles, as well as the standard deviations of the relative angles, agree well in general with the spectral simulations published previously. The fluctuations of relative orientations help rationalize why orientation selectivity effects are minimal at X-band frequencies, but observable at the Q-band for such labels. In summary, the results show that by combining the experimental results with MD simulations precise information about protein conformations as well as flexibility can be obtained.

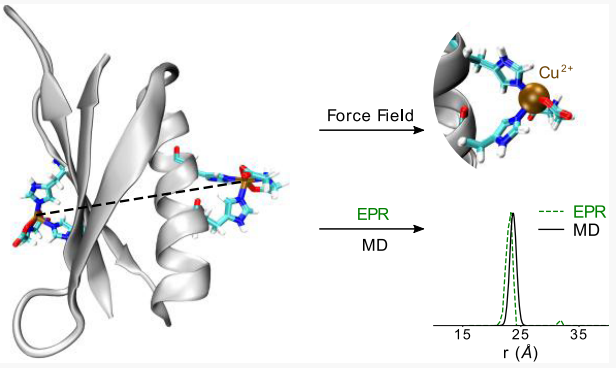

INTRODUCTION

Pulsed electron paramagnetic resonance (EPR) techniques[1−9] that probe nanometer-range distance constraints have become powerful methods to determine macromolecular structure and conformational changes even in large-membrane proteins and in protein−protein and nucleic acid complexes.[10−25] Such techniques involve the measurement of the dipolar interaction between unpaired electron spins of EPR reporters that are often site specifically incorporated in macromolecules. The standard reporter for proteins involves the site-directed spin labeling of cysteine residues with a nitroxide label, most commonly 1-oxyl-2,2,5,5-tetramethylpyrroline-3-methylmethanethiosulfonate (MTSL).[26] The unpaired electron in MTSL is delocalized in the N−O bond of the pyrrole moiety, which is separated from the C_α of the protein residue by five freely rotatable bonds. As a result, distance measurements using MTSL lead to broad distance distributions due to the intrinsic flexibility of the linker. As such, translating the nitroxide distance distributions to protein backbone fluctuations is still ambiguous.[27,28] Alternative nitroxide labels that are more rigid, such as the bifunctional label, have also been developed.[15,29,30] But such rigid labels come at a cost of complex schemes required to introduce the labels in the proteins. In addition, the reliance on cysteine limits application to many proteins, such as kinases, which typically have functional, nonmodifiable cysteines. Besides developing better nitroxide labels, significant efforts have also been made to relate nitroxide conformational dynamics to protein backbone fluctuations using computational techniques.[31−33] Despite such efforts, the accurate prediction of protein backbone fluctuations from distance measurements still remains a challenge. Therefore, efforts toward the development of small and rigid spin labels for precise distance measurements have been a key priority.

Metal-based spin labels have become a promising alternative.[34−36] Along with nitroxides, they can also serve the purpose of orthogonal labeling. One such metal-based labeling technique that has shown great promise is the double-histidine (dHis) Cu^{2+}-binding motif.[37] The dHis motif involves the strategic placement of two histidine residues in the i and $i + 4$ positions for an α-helix and i and $i + 2$ positions for a β-sheet site for chelation to the Cu^{2+}-ion. The labeling technique, thus,

Received: January 27, 2020
Revised: March 16, 2020
Published: March 17, 2020

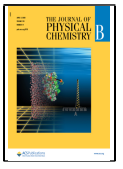

https://dx.doi.org/10.1021/acs.jpcb.0c00739
J. Phys. Chem. B 2020, 124, 2788−2797

does not rely on chemical conjugation with a cysteine residue, which provides another handle for labeling proteins. To ensure specific binding of Cu^{2+} solely to the dHis motif, Cu^{2+} is introduced as a complex with chelating ligands such as iminodiacetic acid (IDA)[37,38] or nitrilotriacetic acid (NTA).[39] These copper complexes show high binding affinity to the dHis motif, with an apparent dissociation constant as low as submicromolar.[40]

Being simultaneously bound to the Cu^{2+} complex, the two histidine side chains have very limited mobility, thereby making dHis−Cu^{2+}−IDA/NTA much more rigid than the standard nitroxide labels. As a result, distance measurements performed using the dHis−Cu^{2+} labeling scheme have provided significantly narrower distance distributions compared to its nitroxide counterparts.[37,41] The rigid dHis−Cu^{2+} label has shown significantly improved resolution, capable of readily measuring structural constraints in two or more distinct functional states of a protein present simultaneously in solution.[41,42] In addition, the technique has opened up new avenues such as determination of the precise and facile location of a native paramagnetic metal ion within a protein[43] and measurement of the relative orientations of two spin-labeled protein sites.[44] These results provide impetus for further development of the dHis−Cu^{2+} labeling technique, especially from a computational aspect to exploit the full potential of the label.

Several methods such as ab initio calculations, molecular dynamics (MD), Monte Carlo simulations, and rotamer libraries are available for capturing the behavior of the nitroxide spin labels when incorporated inside a protein or nucleic acids. For dHis−Cu^{2+}−IDA/NTA, one such effort has been made by incorporating a library of rotamers based on the conformational space of the label in the multiscale modeling of the macromolecular systems (MMM) software.[45] EPR distance constraints obtained using the dHis−Cu^{2+} motif in conjunction with the elastic network modeling in MMM have been able to generate models of protein conformations in different functional states.[41] Such coarse-grained modeling helps to visualize large-scale conformational exchange or structural fluctuations that occur on a slower time scale (e.g., milliseconds).

However, if one needs to view backbone fluctuations, side-chain vibrations, or rotamer exchange, which occur in the pico- to nanosecond range, then more detailed modeling is required. The most common way of capturing such atomic details of the macromolecules is by performing molecular dynamics (MD) simulations. MD simulations in combination with EPR distance constraints have been able to elucidate conformational distributions of biomacromolecules, ascertain the validity of structural models as well as refine protein structures, obtain conformations in different functional states, and probe the types of interactions between atoms.[46−56] However, the availability of high-quality molecular mechanics models for Cu^{2+}−IDA or Cu^{2+}−NTA is a prerequisite for MD simulations.

In this work, we have developed force field parameters for Cu^{2+}−IDA and Cu^{2+}−NTA complexes to be used for MD simulations on dHis-labeled protein systems. High-level density functional theory (DFT) calculations were first performed to build the optimized geometry of the spin labels. Consequently, appropriate bond lengths, bond angles, dihedral angles, partial charges, and force constants were developed for the Cu^{2+}−IDA and Cu^{2+}−NTA labels. Finally, we incorporated the spin labels on a protein with two dHis motifs. From the trajectories of the MD simulations, we obtained the Cu^{2+}−Cu^{2+} distance distribution, which we then compared to the experimental results. Overall, in combination with EPR and MD, we show that the dHis−Cu^{2+} motif can indeed provide precise information about protein conformation and flexibility.

METHODS

Protein System Setup. The protein of interest was the B1 immunoglobulin-binding domain of protein G (GB1). We used the crystal structure (PDB: 4WH4)[37] where the sites 6 and 8 on a β-sheet and sites 28 and 32 on an α-helix were histidine residues. Crystallographic water molecules were removed. For the 15H/17H/28H/32H GB1 mutant, we generated the initial structure from PDB: 4WH4 through computational mutagenesis. Since the histidine mutations on the β-sheet are now on sites 15 and 17, we mutated residues Glu15 and Thr17 into histidine. Simultaneously, the histidine residues at sites 6 and 8 in the crystal structure was replaced with residues isoleucine and asparagine, respectively, based on the wild-type GB1 sequence. The tleap program in Amber was used to generate the histidine side chains at sites 15 and 17 and add the missing H atoms to each residue.[57]

For both protein mutants, proper rotamers of dHis were chosen from PYMOL for the incorporation of Cu^{2+}−IDA or Cu^{2+}−NTA.[58] dHis−Cu^{2+}−IDA or dHis−Cu^{2+}−NTA was aligned to the dHis sites of the proteins.

Molecular Mechanics Force Field (MMFF) Parameterization. Transferability, compatibility, and high accuracy are the main features of a high-quality MMFF. We derived the force field parameters for the Cu^{2+} coordination complexes to be compatible with AMBER additive force fields including ff14SB[59] and a general AMBER force field (GAFF).[60] Two model compounds, bis(imidazole)−Cu^{2+}−NTA and bis(imidazole)−Cu^{2+}−IDA, as shown in Figure 1, were applied to derive force field parameters. The van der Waals parameter of Cu^{2+} in coordinated complexes was first derived using ionization potential (0.283939 eV) and atomic polarizability (6.2 $Å^{-3}$) of Cu^{2+}. Then, the radius parameter was further adjusted using a regression equation. More details on van der

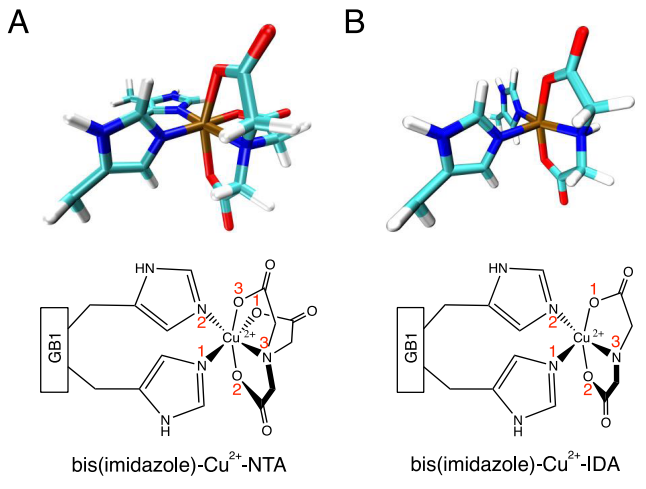

Figure 1. Top panel shows the DFT-optimized structures of (A) bis(imidazole)−Cu^{2+}−NTA (B) and bis(imidazole)−Cu^{2+}−IDA. Cu^{2+} center is shown in brown. Bottom panel shows the two-dimensional (2D) representation of bis(imidazole)−Cu^{2+}−NTA and bis(imidazole)−Cu^{2+}−IDA, respectively.

https://dx.doi.org/10.1021/acs.jpcb.0c00739
J. Phys. Chem. B 2020, 124, 2788−2797

Table 1. Structure Comparison of Bis(imidazole)−Cu^{2+}−NTA[73] and Bis(imidazole)−Cu^{2+}−IDA[71] of Crystal Structures, DFT-Optimized Structure Published by Ghosh et al.,[45] and the Optimized Structure in This Work[a]

bond (Å) or angle (deg)	crystal A[73]	MMM A[45]	QM A	bond (Å) or angle (deg)	crystal B[71]	MMM B[45]	QM B
N1−Cu^{2+}	1.988	2.033	2.042	N1−Cu^{2+}	1.987	2.216	2.309
N2−Cu^{2+}	2.006	2.034	2.063	N2−Cu^{2+}	2.001	2.012	2.004
N3−Cu^{2+}	2.257	2.360	2.156	N3−Cu^{2+}	2.085	2.057	2.029
O1−Cu^{2+}	1.943	1.986	1.982	O1−Cu^{2+}	1.956	2.011	2.011
O2−Cu^{2+}			2.408	O2−Cu^{2+}	2.225	2.014	2.008
O3−Cu^{2+}	1.986	2.027	2.423	O3−Cu^{2+}			
N1−Cu^{2+}−N2	89.2	93.2	92.7	N1−Cu^{2+}−N2	92.1	101.4	101.1

[a]Structures and labels of atoms of bis(imidazole)−Cu^{2+}−NTA/IDA are shown in Figure 2. Distances between atoms and the bond angle of bis(imidazole)−Cu^{2+}−NTA are shown in the left four columns, referred to as A; distances between atoms and the bond angle of bis(imidazole)−Cu^{2+}−IDA are shown in the right four columns, referred to as B. Crystal A/B represents the crystal structures of bis(imidazole)−Cu^{2+}−NTA/IDA. MMM A/B represents the optimized structures by Ghosh et al. QM A/B represents the optimized structures from this work.

Waals parameterization, partial changes, atom types, and parameters involved are provided in the Supporting Information, in a standard format.[61−63] The atomic charges were derived using the RESP program[64] to fit the HF/6-31G* electrostatic potentials after the geometries were optimized at B3LYP/6-311++G(d,p) level, with the solvent effect being taken into account using the polarizable continuum model implemented in the GAUSSIAN 16 software package.[65] We chose B3LYP to be more consistent with the established protocols in AMBER force field development. The justification of our choice of quantum mechanical (QM) method is available in the Supporting Information.

Three residue topologies, representing bis(imidazole)−Cu^{2+}−NTA, bis(imidazole)−Cu^{2+}−IDA, and the main-chain part of the HIE residue (i.e., histidine with hydrogen on the epsilon nitrogen), were prepared using the residuegen program in the Antechamber package.[66] The last residue is needed as the partial charges of the HIE side chain were recalculated using the model compounds while those of the main-chain atoms remain unchanged. The two model compounds of Cu^{2+} complexes were assigned ff14SB atom types and the substitutes of the missing the force field parameters came from GAFF. However, as expected, there was no substitute available for force parameters involving Cu^{2+}. The following describes the strategies of deriving the missing force field parameters. The equilibrium bond length and bond angle values were obtained by doing statistical analyses on the B3LYP/6-311++G(d,p)-optimized geometries. The force constants of bond stretching and bond angle bending were calculated using an empirical formula described elsewhere.[60] The two parameters for Cu^{2+} to be used in the force constant calculations were derived by minimizing the differences between the vibrational frequencies calculated by ab initio and normal mode analyses on the developed molecular mechanics models. We applied a weight to each vibration mode depending on the contribution of Cu^{2+} in this mode—the larger the contribution of Cu^{2+}, the larger the weight for this mode. The torsional angle parameters with Cu^{2+} being at the second or third position were set to 0.0, as usually done for metallic atom types in MMFF.[67]

MD Simulations. All proteins were simulated with the ff14SB AMBER force field.[57] Solvent waters were treated with the TIP3P water model.[68] The spin-labeled protein was solvated in a cubic water box. The box size was roughly 60 $Å^3$ for spin-labeled GB1. Chloride and sodium ions were added to neutralize the systems with a final concentration of 150 mM. All simulations were performed using the pmemd program in the AMBER18 software package. The solvated systems were energy-minimized with a harmonic restraint force constant applied to the main-chain protein. The restraint was gradually released from 20, 10, 5, and 1 to 0 kcal/(mol $Å^2$) over a total of 12 000 steps. The minimized structures were then equilibrated with a Berendsen barostat at 298.15 K for 3.2 ns with progressively decreasing harmonic restraint force constants of 20, 10, 5, and 1 kcal/(mol $Å^2$).[69] Each system was then gradually heated from 0 to 298.15 K. The time step for integration of motions was 2 fs for the heating, equilibrium, and the following production phases. The temperature was maintained at 298.15 K for the production simulation. Periodic boundary conditions along with particle mesh Ewald (PME) were applied to accurately account for the long-range electrostatic interactions. The temperature was controlled with the Langevin thermostat using a collision frequency of 5.0 ps^{-1}. The pressure was maintained at 1 atm with a relaxation time of 1.0 ps. SHAKE was used to restrain all bonds involving hydrogen. A nonbonded cutoff of 10 Å was applied. All systems reached equilibrium after 2 ns, and the total simulation time was 200 ns. To eliminate the possible influence of the starting conformation, five independent MD runs were performed for the Cu^{2+}−NTA-labeled 6H/8H/28H/32H and 15H/17H/28H/32H GB1 mutants using the equilibrated structures. Each of the independent simulations was assigned initial velocities randomly, using a random number generator seed.

DEER Experiment. To acquire distance information between labeled sites of Cu^{2+}−IDA-labeled 15H/17H/28H/32H GB1 mutants, the DEER experiment was performed. The DEER experiment was performed with a Bruker E580 spectrometer and a 1 kW amplifier at an X-band frequency at 20 K. The resonator was over-coupled to a bandwidth of 200 MHz. A four-pulse DEER with 16-step phase cycling was carried out with the sequence $(\pi/2)\ \upsilon_A - \tau - (\pi)\ \upsilon_A - \tau + T - (\pi)\ \upsilon_B - \tau_2 - T - (\pi)\ \upsilon_A - \tau_2 -$ echo. A square pulse of 24 ns at pump frequency (υ_B) was used. Observer pulses were square-shaped with a π pulse length of 30 ns. The step size was 10 ns and incremented over 139 points. DeerAnalysis2018 was used to analyze the data.[70]

RESULTS AND DISCUSSION

So far, the MMM software has been able to generate the rotamer libraries for Cu^{2+}−NTA and Cu^{2+}−IDA spin labels.[45] In this software, rotamers of Cu^{2+}−NTA/IDA are computed and incorporated into the crystal structures of the protein. Furthermore, the program uses elastic network modeling and EPR distances in different functional states to calculate

https://dx.doi.org/10.1021/acs.jpcb.0c00739
J. Phys. Chem. B 2020, 124, 2788−2797

structural models of the protein in each state. Such analysis can provide perspective on the large-amplitude changes in protein conformation that typically occur in the microsecond−millisecond range. However, to view protein backbone fluctuations occurring in the pico- to nanosecond range, molecular dynamics simulations are useful.

To accurately model our Cu^{2+} labels, we developed MMFF parameters for bis(imidazole)−Cu^{2+}−NTA and bis(imidazole)−Cu^{2+}−IDA to replicate the dHis−Cu^{2+}−NTA/IDA label. We first used the B3LYP/6-311++G(d,p) basis set to optimize the geometry of the Cu^{2+} label structures, as described in the Methods section. The optimized structures of bis(imidazole)−Cu^{2+}−NTA and bis(imidazole)−Cu^{2+}−IDA are shown in Figure 1, and the ab initio-optimized bond angles and bond lengths are summarized in Table 1. For bis(imidazole)−Cu^{2+}−IDA, the Cu^{2+} is coordinated to the two nitrogen atoms of the imidazole moieties and one nitrogen and two oxygen atoms of the IDA. These results are consistent with prior EPR results[38,39] and with the crystallographic results of a Cu^{2+} complexed with IDA and two imidazole ligands.[71] The results are also similar to the previously DFT-optimized models of Cu^{2+}−IDA that were incorporated in the MMM software.[45] Notably, our optimized structure has only five coordinating atoms to the Cu^{2+}. Typically, most common Type 2 Cu^{2+} complexes exist with a six-coordinate octahedral geometry.[72] We attempted to add one water molecule so that the coordination number becomes six for bis(imidazole)−Cu^{2+}−IDA. However, this water molecule could not be kept in a proper position and the distance between Cu^{2+} and oxygen of the water was larger than 4.0 Å after the optimization.

The bis(imidazole)−Cu^{2+}−NTA-optimized structure shows a six-coordination environment of Cu^{2+}, involving two nitrogens from the imidazoles and one nitrogen and three oxygen atoms from the NTA ligand. The results are consistent with EPR[39] and the results from the crystal structure of Cu^{2+} complexed with NTA and two imidazole molecules.[73] However, the optimized structure does not agree with that used in MMM. The MMM model is a penta-coordinated Cu^{2+} containing keto-linked imidazole molecules. Such keto-bridging between imidazole moieties was meant to facilitate formation of a six-coordinate Cu^{2+} complex and likely does not completely represent the native double-histidine nature of Cu^{2+}−NTA.

The molecular mechanics models for bis(imidazole)−Cu^{2+}−NTA and bis(imidazole)−Cu^{2+}−IDA were developed following the philosophy of AMBER additive force field development. The average unsigned errors of the vibration frequencies are 36.41 and 33.78 cm^{-1} for the NTA and IDA model compounds, respectively. The corresponding root-mean-square errors of 65.2 and 61.4 cm^{-1} are also much smaller than the average error of GAFF-predicted vibrational frequencies. We evaluated the two model compounds by running 2000 step minimization and 1 nanosecond MD simulations using a generalized Born model (igb = 1) to account for the solvent effect.[74] The root-mean-square deviations (RMSDs) between the minimized and ab initio geometries are 0.43 and 0.58 Å for the NTA and IDA model compounds, respectively. Both MD simulations are very stable, and 500 snapshots were collected for plotting RMSD ∼ simulation time curves. The heavy-atom RMSDs of 500 snapshots are 1.11 ± 0.20 and 1.42 ± 0.27 Å for the NTA and IDA model compounds, respectively. These results are very reasonable for large model compounds like bis(imidazole)−Cu^{2+}−NTA and bis(imidazole)−Cu^{2+}−IDA. The residue topologies and force field parameter files for both compounds are provided in the Supporting Information.

After optimizing the geometries and developing force fields for the dHis−Cu^{2+} complexes, we must put them in the context of a protein to perform relevant MD simulations. For MD analysis, we considered two spin-labeled mutants of GB1. GB1 is a stable, globular protein[75,76] with both α-helix and β-sheet secondary structures. GB1 has been well characterized by EPR, NMR, and X-ray crystallography.[77−85] This thorough understanding makes GB1 an appropriate model system for testing the feasibility of performing MD simulations on spin-labeled proteins with spin labels located at different secondary structures. In this work, we used the 6H/8H/28H/32H and 15H/17H/28H/32H mutants of GB1. The β-sheet dHis sites were 6H/8H and 15H/17H, while the α-helix dHis site was 28H/32H. All structures were built starting from the initial GB1 crystal structure (PDB: 4WH4). The B3LYP-optimized structures of Cu^{2+}−IDA or Cu^{2+}−NTA were then attached to the dHis sites.

Five independent MD runs of 200 ns were performed to reduce the influence of the starting conformation. The distance between the two Cu^{2+} centers was calculated for all MD frames saved every 10 ps of the MD trajectory. Figure 2 shows the distance distributions obtained from one of the MD runs compared to the experimental distributions, as well as the distributions estimated using the MMM software. The four other independent MD runs gave very similar results (Figure S3). The experimental EPR distance measurements on Cu^{2+}−NTA-labeled 6H/8H/28H/32H and 15H/17H/28H/32H GB1, Cu^{2+}−IDA-labeled 6H/8H/28H/32H GB1 were previously published.[38,39] The validations to these distance distributions have been provided in Figure S2. The distance measurement for Cu^{2+}−IDA-labeled 15H/17H/28H/32H GB1 was obtained and validated for this work (data shown in Figure S2).

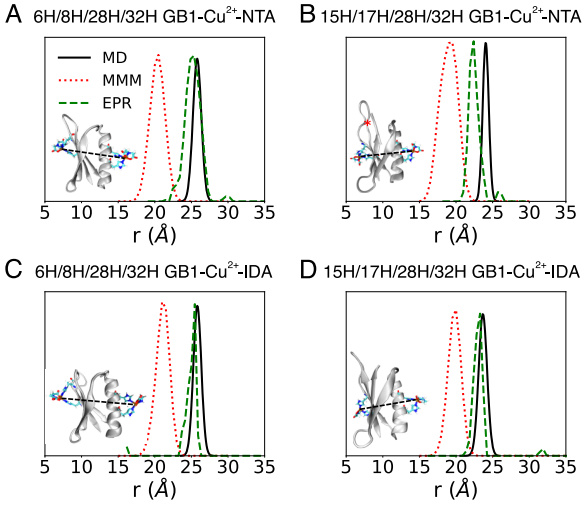

Figure 2. Comparison of distance distributions for Cu^{2+}−NTA-labeled 6H/8H/28H/32H GB1 (A) and 15H/17H/28H/32H GB1 (B), Cu^{2+}−IDA-labeled 6H/8H/28H/32H GB1 (C) and 15H/17H/28H/32H GB1 (D) with the solution structure shown as cartoons in the bottom left of each panel. The distributions of the Cu^{2+}−Cu^{2+} distances obtained from EPR measurements, MMM simulations, and 200 ns MD simulations are shown by these green dashed lines, red dotted lines, and black solid lines, respectively.

https://dx.doi.org/10.1021/acs.jpcb.0c00739
J. Phys. Chem. B 2020, 124, 2788−2797

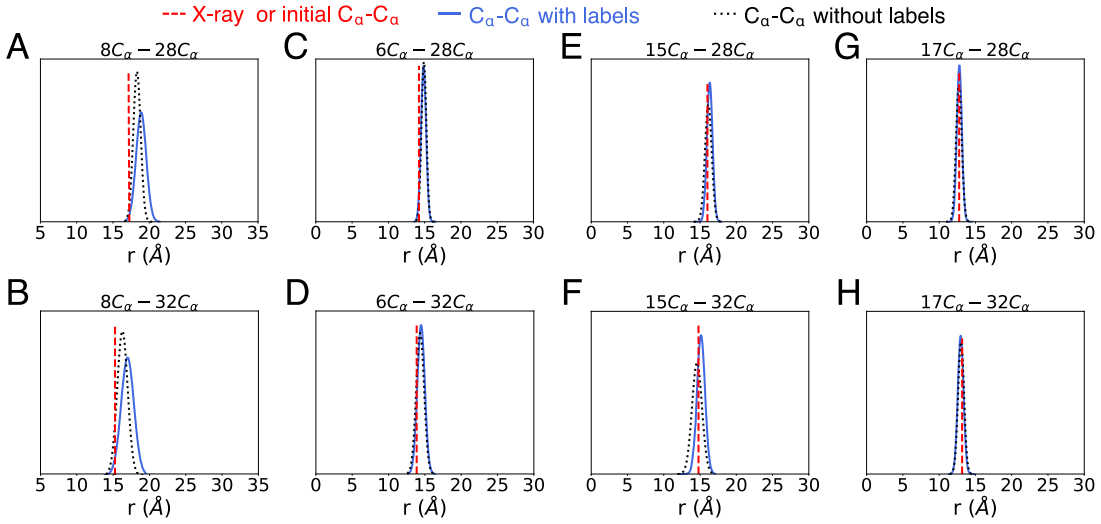

Figure 3. Distributions of C_α–C_α distance of the spin-labeled sites for 6H/8H/28H/32H and 15H/17H/28H/32H GB1 with Cu^{2+}–NTA labels (blue solid); the corresponding C_α–C_α distance distributions without spin labels (black dotted). The C_α–C_α distances from the crystal structure or the initial structure for simulation are shown as red dashed vertical lines. C_α–C_α distances for 6H/8H/28H/32H between (A) sites 8 and 28, (B) sites 8 and 32, (C) sites 6 and 28, and (D) sites 6 and 32. C_α–C_α distances for 15H/17H/28H/32H between (E) sites 15 and 28, (F) sites 15 and 32, (G) sites 17 and 28, and (H) sites 17 and 32.

For Cu^{2+}–NTA-labeled 6H/8H/28H/32H and 15H/17H/28H/32H GB1 mutants, the most probable distances from MD simulations agreed well with the EPR experiments. The difference between MD simulations and DEER experiments was within the experimental error and the resolution of the crystal structure (2.2 Å for 4WH4). Overall, the MD simulations showed significantly improved agreement with the experimental EPR data than MMM. The most probable distances from MD agree within 1–2 Å, whereas the MMM distributions are within 4–5 Å. Additionally, the distribution width of the MD simulations is in better agreement with the experimental data within 1 Å, whereas the MMM distribution width is larger than the EPR experimental distribution width by 2–4 Å. Distance distributions generated using the Cu^{2+}–IDA label showed similar distance distributions as the Cu^{2+}–NTA-labeled systems (Figure 2C,D).

As expected, the solution structures of the proteins with Cu^{2+}–NTA labels compared to those with Cu^{2+}–IDA labels do not show significant difference during simulation. The improved predictions of distances from the MD simulations compared to the previously reported MMM results are likely due to (1) the inclusion of protein dynamics; (2) the use of the detailed atomistic force field ff14SB with the explicit solvent to calculate forces and propagate dynamics for the spin-labeled protein; and (3) the optimized structure of bis(imidazole)–Cu^{2+}–NTA with more realistic coordination environment to Cu^{2+}.

Based on these factors, it is unsurprising that MD provides a closer agreement with the experimental EPR results than MMM. However, both techniques are still valuable and are complementary when used together. The true strength of MMM lies in that one can use sparse distance constraints to obtain model structures of proteins in different functional states. These conformational changes from one functional state to another involve large-amplitude slow motions, which, for large proteins, are often not accessible to NMR, crystallography, or conventional MD simulations. Another advantage of the MMM software is that it only takes minutes to a few hours to generate protein conformations in different functional states. On the other hand, a 200 ns standard MD simulation on a moderate-sized protein will normally take a few days to a few weeks depending on the type of supercomputing resources available. The results in Figure 2 suggest that MMM can be used to obtain initial models of such functional states that can be subsequently refined by atomistic MD simulations.

To further verify the robustness of the force fields, we performed 200 ns MD simulations on 6H/8H/28H/32H GB1 15H/17H/28H/32H GB1 without the Cu^{2+} labels. Figures 3 and S4 show the C_α–C_α distance distributions of the labeled sites sampled from the MD simulations with the labels (blue solid line) and without the labels (black dotted line). The C_α–C_α distances from the crystal structure[37] or the initial structure are shown as red dashed vertical lines. The most probable C_α–C_α distances from the MD simulations of labeled proteins are in reasonable agreement with those obtained for the unlabeled protein with a difference less than 1 Å, suggesting that the in silico formation of the coordination compound with the Cu^{2+} labels does not induce large changes in protein dynamics and structure. Site 8-related distances show slightly broader distributions, possibly due to the fact that it is located at the edge of the β-sheet and is more flexible, whose location is indicated in the inset of Figure 2B as a red asterisk, whereas sites 6, 15, and 17 are located in the middle of the β-sheet. The data also validate the use of EPR distance measurements and the MD simulations to infer site-specific information on protein flexibility.

To visualize the atomic properties of the dHis–Cu^{2+} DEER experiments, Figure 4A plots the predicted Cu^{2+} positions of Cu^{2+}–NTA-labeled 6H/8H/28H/32H GB1 from MD simulations, compared to those obtained from MMM using a space-filling model in Figure 4B. Similar to MMM predictions, MD simulations of Cu^{2+}–NTA-labeled 6H/8H/28H/32H GB1 show very localized Cu^{2+} positions, indicating a narrow distance distribution between the labeled sites. Figure 4C shows the predicted conformers of the common nitroxide label, R1, by MMM. The comparison of copper positions (Figure 4A,B) versus R1 positions (Figure 4C) dramatically illustrates the rigidity of the Cu^{2+} and the power and potential

https://dx.doi.org/10.1021/acs.jpcb.0c00739
J. Phys. Chem. B 2020, 124, 2788–2797

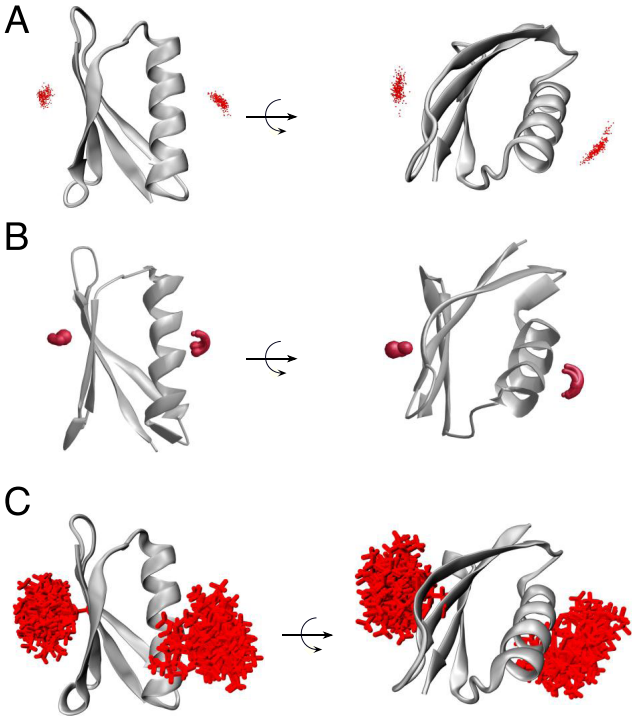

Figure 4. Predicted Cu^{2+} spatial distributions of Cu^{2+}–NTA-labeled 6H/8H/28H/32H GB1 by MD simulations (A), by MMM (B) and nitroxide label R1 distribution by MMM (C).

of Cu^{2+}-based distance measurements to accurately resolve a myriad of protein structural and conformational aspects, such as conformational changes, quaternary structural arrangements, protein–protein interactions, and more.

In addition to the distance information, the MD simulations also help explain orientational effects in Cu^{2+}–dHis-based DEER. In DEER, orientational effects are due to the excitation of only a fraction of the total EPR spectrum, which can sometimes result in the selection of a small subset of all possible molecular orientations.[44,86−93] Such orientational effects cause DEER experiments performed at different magnetic fields to show distinctly different signals. For nitroxides, orientational selectivity is usually not observed at the X-band (~9.5 GHz) due to the flexibility of the linker and the interplay of hyperfine anisotropies and g-splittings. Both factors effectively mix orientations across the spectrum such that even the limited excitation of DEER effectively samples multiple molecular orientations.[34,94] Ultra-wide-band excitation can also overcome this limitation by effectively exciting the entire EPR spectrum.[95] On the other hand, highly rigid labels can exhibit orientational selectivity and can be used to measure orientational information.[88,92,96−99]

For dHis-based Cu^{2+}-labels, orientational effects are also uncommon at X-band frequencies, despite the rigidity of the label.[37−39,44] We have previously postulated that the g-tensor of the Cu^{2+} has a distribution of orientations, which may act to randomize the selected molecular orientations.[89]

The MD results provide evidence for this postulate and allow us to examine the role of molecular and residual fluctuations in the orientational selectivity of rigid Cu^{2+}-based systems. First, the Cu^{2+} coordination fluctuates during the course of the MD simulations; for example, the distance between Cu^{2+} and the imidazole nitrogen changes by ~30% with a range of 1.74–2.39 Å and an average distance of 2.07 Å. The high plasticity of the Cu^{2+} coordination leads to a range of g-tensor values, which we calculated for a range of conformations in the MD simulations using the CAM-B3LYP QM method and 6-311++G(d,p) basis set. The g-tensor values changed by up to 10% due to changes in the ligand to Cu^{2+} distances and the torsion angles. More importantly, changes in torsion angles and coordination lead to a large change in the orientations of $g_{\|}$. Second, rotameric fluctuations of the side chain lead to changes in g-tensor directions. Together these effects reduce orientational selectivity.

Here we analyzed just the effects of rotameric fluctuations. Figure 5A shows the coordination environment of Cu^{2+}, with

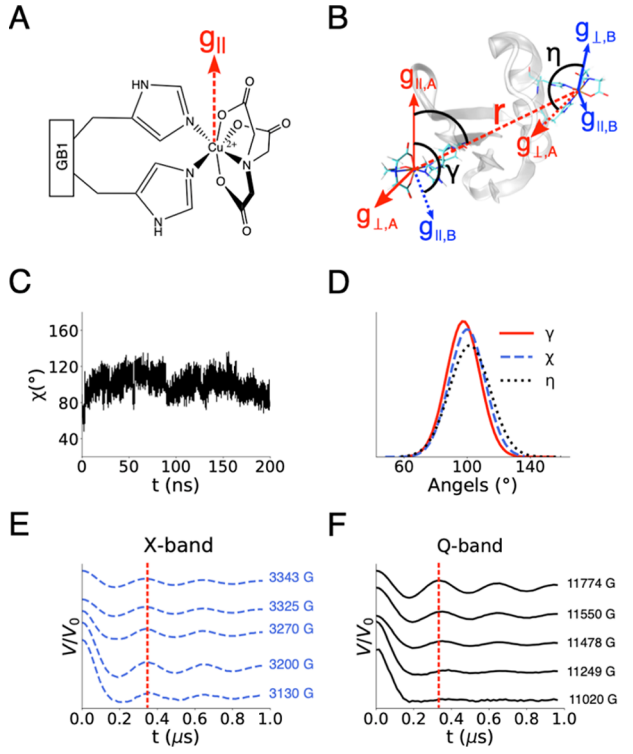

Figure 5. (A) Coordination environment of Cu^{2+} binding to NTA and dHis. The imidazole nitrogens bind to Cu^{2+} equatorially, leading to the definition of $g_{\|}$ being perpendicular to the equatorial plane. (B) The principal axes for spin A (red) and spin B (blue) are defined, with relative orientations between the two spins indicated by three angles, γ, χ, and η. (C) The angle χ as a function of simulation time. (D) The distributions of angle γ, χ, and η. (E) and (F) Simulated DEER signal at the selected fields at X-band frequency and Q-band frequency, respectively. The red dashed line indicates the first period of the modulations at all fields of the X-band or at 11774 G ($g_{\|}$) of the Q-band. The orientational selectivity is mostly washed out due to the σ being above 10.0° at the X-band frequency, whereas it is overt at the Q-band frequency.

$g_{\|}$ perpendicular to the equatorially coordinated ligands. Figure 5B shows the molecular reference frame of the dHis–Cu^{2+}-labeled GB1 and the three angles that define the relative orientations of the two Cu^{2+}. We calculated each angle across every frame of our MD results for the Cu^{2+}–NTA-labeled 6H/8H/28H/32H GB1. Figures 5C and S5A,B show χ, γ, and η as a function of time. Note that χ was shown to have the highest influence on the resultant DEER signals at the X-band.[89] Interestingly, all angles sample a broad range of values, with the standard deviations in angles being greater than 10°, as shown

https://dx.doi.org/10.1021/acs.jpcb.0c00739
J. Phys. Chem. B 2020, 124, 2788−2797

in Figure 5D. More precisely, the observed mean angles and standard distributions in MD are 97.5°; 10.6° (mean; standard deviation) for γ; 100.0°; 11.3° for χ, and 101.6°; 12.9° for η. Previous experimental Q-band DEER data was consistent with 75°; 10° for γ, 80°; 10° for χ, and 22.5°; 10° for η.[44] Notably, we have reasonable agreement between the MD and previously reported values for χ and γ, although there is a discrepancy in the values of η.

More importantly, the MD results clearly show that minor fluctuations in the dihedral angles of the side chains and Cu^{2+} coordination lead to an appreciable orientational distribution between the two Cu^{2+} ions, even though the metal ions are relatively fixed. To emphasize this point, we simulated DEER signals at both the X-band and Q-band using the set of angles obtained from MD, as shown in Figure 5E,F, respectively. Using our angles and, more importantly, our standard deviations as determined from MD, it is clear that orientational effects are washed out at the X-band, but not at the Q-band. It is also notable that the X-band simulations agree well with the previous results, but the modulation frequencies of the Q-band simulations do not, as shown in Figure S6A,B. This is likely due to the discrepancy in the η angle, which shows that while χ may be the most influential at the X-band the influence of all three angles contributes to the Q-band signal. These results as a whole not only present MD simulations as another complementary tool in the orientational analysis of dHis–Cu^{2+} systems but also provide clear evidence that the absence of orientational selectivity in Cu^{2+} at the X-band is due to molecular fluctuations, imparting a distribution in g-tensor orientations. More practically, these results suggest that X-band DEER can be used to readily measure distance distributions using the dHis label. On the other hand, the Q-band DEER may provide information on the relative orientations of different secondary structure elements.[44]

CONCLUSIONS

In conclusion, we have developed force field parameters for the spin labels dHis–Cu^{2+}–NTA and dHis–Cu^{2+}–IDA. Molecular mechanics modeling based on the newly developed force field parameters also shows remarkable agreement with the EPR measurements. The MD simulations indicate that protein backbone flexibility is similar both with and without the label, which suggests that the force fields are robust and, importantly, that the spin label does not perturb protein dynamics. In addition, the MD simulations provide insight into the localized spatial distribution of the Cu^{2+} labels, which leads to precise structural constraints for biophysical measurements. This work also confirms the hypothesis that the label exhibits sufficient orientational distribution such that orientational selectivity is not observed at the X-band but achievable at the Q-band frequency. Therefore, distance measurements using such dHis labels can be readily performed at the X-band, while Q-band DEER may provide angular information. Finally, the distance measurements using the dHis label can be combined with MD simulations to refine protein structure, gain insights into protein dynamics, and to characterize protein functions.

ASSOCIATED CONTENT

Supporting Information

The Supporting Information is available free of charge at https://pubs.acs.org/doi/10.1021/acs.jpcb.0c00739.

Force field parameter files and residue topologies for bis(imidazole)–Cu^{2+}–NTA and bis(imidazole)–Cu^{2+}–IDA, van der Waals force field parameterization for Cu^{2+}, justification of our choice of the QM method, DEER data on Cu^{2+}–IDA-labeled 15H/17H/28H/32H GB1 and validations for distance distributions, Cu^{2+}–Cu^{2+} distance distributions from each 200 ns MD run for two spin-labeled systems, distributions of C_α–C_α distance of the spin-labeled sites for Cu^{2+}–IDA-labeled GB1 mutants, the angles γ and η as a function of simulation time, simulated DEER data based on MD simulations and experiments (PDF)

AUTHOR INFORMATION

Corresponding Authors

Junmei Wang − *Department of Pharmaceutical Sciences, University of Pittsburgh, Pittsburgh, Pennsylvania 15206, United States*; Phone: 412 383 3268; Email: junmei.wang@pitt.edu

Sunil Saxena − *Department of Chemistry, University of Pittsburgh, Pittsburgh, Pennsylvania 15260, United States*; orcid.org/0000-0001-9098-6114; Phone: 412 624 8680; Email: sksaxena@pitt.edu

Authors

Xiaowei Bogetti − *Department of Chemistry, University of Pittsburgh, Pittsburgh, Pennsylvania 15260, United States*

Shreya Ghosh − *Department of Chemistry, University of Pittsburgh, Pittsburgh, Pennsylvania 15260, United States*

Austin Gamble Jarvi − *Department of Chemistry, University of Pittsburgh, Pittsburgh, Pennsylvania 15260, United States*

Complete contact information is available at: https://pubs.acs.org/10.1021/acs.jpcb.0c00739

Notes

The authors declare no competing financial interest.

ACKNOWLEDGMENTS

This research was supported by the National Science Foundation (NSF MCB-1613007). Simulations were performed with support from the Center for Research Computing at the University of Pittsburgh. The EPR spectrometer was supported by the National Science Foundation (NSF MRI-1725678).

ABBREVIATIONS

EPR, electron paramagnetic resonance; DEER, double electron–electron resonance; NTA, nitrilotriacetic acid; IDA, iminodiacetic acid; QM, quantum mechanical; MD, molecular dynamics; GAFF, a general AMBER force field; MMFF, molecular mechanics force field

REFERENCES

(1) Saxena, S.; Freed, J. H. Double Quantum Two-Dimensional Fourier Transform Electron Spin Resonance: Distance Measurements. *Chem. Phys. Lett.* **1996**, *251*, 102–110.

(2) Borbat, P. P.; Freed, J. H. Multiple-Quantum ESR and Distance Measurements. *Chem. Phys. Lett.* **1999**, *313*, 145–154.

(3) Bonora, M.; Becker, J.; Saxena, S. Suppression of Electron Spin-Echo Envelope Modulation Peaks in Double Quantum Coherence Electron Spin Resonance. *J. Magn. Reson.* **2004**, *170*, 278–283.

(4) Becker, J. S.; Saxena, S. Double Quantum Coherence Electron Spin Resonance on Coupled Cu(II)−Cu(II) Electron Spins. *Chem. Phys. Lett.* **2005**, *414*, 248−252.
(5) Kulik, L. V.; Dzuba, S. A.; Grigoryev, I. A.; Tsvetkov, YuD. Electron Dipole−Dipole Interaction in ESEEM of Nitroxide Biradicals. *Chem. Phys. Lett.* **2001**, *343*, 315−324.
(6) Milikisyants, S.; Scarpelli, F.; Finiguerra, M. G.; Ubbink, M.; Huber, M. A Pulsed EPR Method to Determine Distances between Paramagnetic Centers with Strong Spectral Anisotropy and Radicals: The Dead-Time Free RIDME Sequence. *J. Magn. Reson.* **2009**, *201*, 48−56.
(7) Milov, A. D.; Maryasov, A. G.; Tsvetkov, Y. D. Pulsed Electron Double Resonance (PELDOR) and Its Applications in Free-Radicals Research. *Appl. Magn. Reson.* **1998**, *15*, 107−143.
(8) Jeschke, G.; Pannier, M.; Godt, A.; Spiess, H. W. Dipolar Spectroscopy and Spin Alignment in Electron Paramagnetic Resonance. *Chem. Phys. Lett.* **2000**, *331*, 243−252.
(9) Pannier, M.; Veit, S.; Godt, A.; Jeschke, G.; Spiess, H. W. Dead-Time Free Measurement of Dipole−Dipole Interactions between Electron Spins. *J. Magn. Reson.* **2000**, *142*, 331−340.
(10) Stone, K. M.; Townsend, J. E.; Sarver, J.; Sapienza, P. J.; Saxena, S.; Jen-Jacobson, L. Electron Spin Resonance Shows Common Structural Features for Different Classes of Eco RI-DNA Complexes. *Angew. Chem., Int. Ed.* **2008**, *47*, 10192−10194.
(11) Grote, M.; Polyhach, Y.; Jeschke, G.; Steinhoff, H. J.; Schneider, E.; Bordignon, E. Transmembrane Signaling in the Maltose ABC Transporter MalFGK2-E. Periplasmic MalF-P2 Loop Communicates Substrate Availability to the ATP-Bound MalK DIMER. *J. Biol. Chem.* **2009**, *284*, 17521−17526.
(12) Hagelueken, G.; Ingledew, W. J.; Huang, H.; Petrovic-Stojanovska, B.; Whitfield, C.; ElMkami, H.; Schiemann, O.; Naismith, J. H. PELDOR Spectroscopy Distance Fingerprinting of the Octameric Outer-Membrane Protein Wza from *Escherichia coli*. *Angew. Chem., Int. Ed.* **2009**, *48*, 2904−2906.
(13) Swanson, M. A.; Kathirvelu, V.; Majtan, T.; Frerman, F. E.; Eaton, G. R.; Eaton, S. S. DEER Distance Measurement Between a Spin Label and a Native FAD Semiquinone in Electron Transfer Flavoprotein. *J. Am. Chem. Soc.* **2009**, *131*, 15978−15979.
(14) Sen, K. I.; Wu, H.; Backer, J. M.; Gerfen, G. J. The Structure of P85ni in Class IA Phosphoinositide 3-Kinase Exhibits Interdomain Disorder. *Biochemistry* **2010**, *49*, 2159−2166.
(15) Fleissner, M. R.; Bridges, M. D.; Brooks, E. K.; Cascio, D.; Kálai, T.; Hideg, K.; Hubbell, W. L. Structure and Dynamics of a Conformationally Constrained Nitroxide Side Chain and Applications in EPR Spectroscopy. *Proc. Natl. Acad. Sci. U.S.A.* **2011**, *108*, 16241−16246.
(16) Drescher, M.; Huber, M.; Subramaniam, V. Hunting the Chameleon: Structural Conformations of the Intrinsically Disordered Protein Alpha-Synuclein. *ChemBioChem* **2012**, *13*, 761−768.
(17) Pornsuwan, S.; Giller, K.; Riedel, D.; Becker, S.; Griesinger, C.; Bennati, M. Long-Range Distances in Amyloid Fibrils of α-Synuclein from PELDOR Spectroscopy. *Angew. Chem.* **2013**, *125*, 10480−10484.
(18) Joseph, B.; Sikora, A.; Bordignon, E.; Jeschke, G.; Cafiso, D. S.; Prisner, T. F. Distance Measurement on an Endogenous Membrane Transporter in *E. coli* Cells and Native Membranes Using EPR Spectroscopy. *Angew. Chem., Int. Ed.* **2015**, *54*, 6196−6199.
(19) Li, Q.; Shen, R.; Treger, J. S.; Wanderling, S. S.; Milewski, W.; Siwowska, K.; Bezanilla, F.; Perozo, E. Resting State of the Human Proton Channel Dimer in a Lipid Bilayer. *Proc. Natl. Acad. Sci. U.S.A.* **2015**, *112*, E5926−E5935.
(20) Puljung, M. C.; DeBerg, H. A.; Zagotta, W. N.; Stoll, S. Double Electron−Electron Resonance Reveals CAMP-Induced Conformational Change in HCN Channels. *Proc. Natl. Acad. Sci. U.S.A.* **2014**, *111*, 9816−9821.
(21) Milikisiyants, S.; Wang, S.; Munro, R. A.; Donohue, M.; Ward, M. E.; Bolton, D.; Brown, L. S.; Smirnova, T. I.; Ladizhansky, V.; Smirnov, A. I. Oligomeric Structure of Anabaena Sensory Rhodopsin in a Lipid Bilayer Environment by Combining Solid-State NMR and Long-Range DEER Constraints. *J. Mol. Biol.* **2017**, *429*, 1903−1920.
(22) Yardeni, E. H.; Bahrenberg, T.; Stein, R. A.; Mishra, S.; Zomot, E.; Graham, B.; Tuck, K. L.; Huber, T.; Bibi, E.; Mchaourab, H. S.; Goldfarb, D. Probing the Solution Structure of the *E. coli* Multidrug Transporter MdfA Using DEER Distance Measurements with Nitroxide and Gd(III) Spin Labels. *Sci. Rep.* **2019**, *9*, No. 12528.
(23) Sahu, I. D.; Dixit, G.; Reynolds, W.; Harding, B.; Jaycox, C.; Faleel, F. D. M.; McCarrick, R. M.; Sanders, C. R.; Lorigan, G. A. Studying Conformation of the Voltage-Sensor Domain (VSD) of the Human KCNQ1 Potassium Ion Channel in Proteoliposomes Using EPR Spectroscopy. *Biophys. J.* **2019**, *116*, 26a.
(24) Fichou, Y.; Eschmann, N.; Han, S. Capturing Conformational Changes of the Tau Protein Upon Aggregation. *Biophys. J.* **2018**, *114*, 429a.
(25) Schmidt, T.; Schwieters, C. D.; Clore, G. M. Spatial Domain Organization in the HIV-1 Reverse Transcriptase P66 Homodimer Precursor Probed by Double Electron-Electron Resonance EPR. *Proc. Natl. Acad. Sci. U.S.A.* **2019**, *116*, 17809−17816.
(26) Hubbell, W. L.; Cafiso, D. S.; Altenbach, C. Identifying Conformational Changes with Site-Directed Spin Labeling. *Nat. Struct. Biol.* **2000**, *7*, 735−739.
(27) Sarver, J. L.; Townsend, J. E.; Rajapakse, G.; Jen-Jacobson, L.; Saxena, S. Simulating the Dynamics and Orientations of Spin-Labeled Side Chains in a Protein−DNA Complex. *J. Phys. Chem. B* **2012**, *116*, 4024−4033.
(28) Fajer, M. I.; Li, H.; Yang, W.; Fajer, Piotr G. Mapping Electron Paramagnetic Resonance Spin Label Conformations by the Simulated Scaling Method. *J. Am. Chem. Soc.* **2007**, *129*, 13840−13846.
(29) Rayes, R. F.; Kalai, T.; Hideg, K.; Geeves, M. A.; Fajer, P. G. Dynamics of Tropopyosin in Muscle Fibers as Monitored by Saturation Transfer EPR of Bi-Functional Probe. *PLoS One* **2011**, *6*, No. e21277.
(30) Sahu, I. D.; McCarrick, R. M.; Troxel, K. R.; Zhang, R.; Smith, H. J.; Dunagan, M. M.; Swartz, M. S.; Rajan, P. V.; Kroncke, B. M.; Sanders, C. R.; Lorigan, G. A. DEER EPR Measurements for Membrane Protein Structures via Bifunctional Spin Labels and Lipodisq Nanoparticles. *Biochemistry* **2013**, *52*, 6627−6632.
(31) Polyhach, Y.; Bordignon, E.; Jeschke, G. Rotamer Libraries of Spin Labelled Cysteines for Protein Studies. *Phys. Chem. Chem. Phys.* **2011**, *13*, 2356−2366.
(32) Hatmal, M. M.; Li, Y.; Hegde, B. G.; Hegde, P. B.; Jao, C. C.; Langen, R.; Haworth, I. S. Computer Modeling of Nitroxide Spin Labels on Proteins. *Biopolymers* **2012**, *97*, 35−44.
(33) Hagelueken, G.; Ward, R.; Naismith, J. H.; Schiemann, O. MtsslWizard: In Silico Spin-Labeling and Generation of Distance Distributions in PyMOL. *Appl. Magn. Reson.* **2012**, *42*, 377−391.
(34) Ji, M.; Ruthstein, S.; Saxena, S. Paramagnetic Metal Ions in Pulsed ESR Distance Distribution Measurements. *Acc. Chem. Res.* **2014**, *47*, 688−695.
(35) Cunningham, T. F.; Shannon, M. D.; Putterman, M. R.; Arachchige, R. J.; Sengupta, I.; Gao, M.; Jaroniec, C. P.; Saxena, S. Cysteine-Specific Cu^{2+} Chelating Tags Used as Paramagnetic Probes in Double Electron Electron Resonance. *J. Phys. Chem. B* **2015**, *119*, 2839−2843.
(36) Goldfarb, D. Pulse EPR in Biological Systems − Beyond the Expert's Courtyard. *J. Magn. Reson.* **2019**, *306*, 102−108.
(37) Cunningham, T. F.; Putterman, M. R.; Desai, A.; Horne, W. S.; Saxena, S. The Double-Histidine Cu^{2+} -Binding Motif: A Highly Rigid, Site-Specific Spin Probe for Electron Spin Resonance Distance Measurements. *Angew. Chem., Int. Ed.* **2015**, *54*, 6330−6334.
(38) Lawless, M. J.; Ghosh, S.; Cunningham, T. F.; Shimshi, A.; Saxena, S. On the Use of the Cu^{2+} −Iminodiacetic Acid Complex for Double Histidine Based Distance Measurements by Pulsed ESR. *Phys. Chem. Chem. Phys.* **2017**, *19*, 20959−20967.
(39) Ghosh, S.; Lawless, M. J.; Rule, G. S.; Saxena, S. The Cu^{2+}-Nitrilotriacetic Acid Complex Improves Loading of α-Helical Double Histidine Site for Precise Distance Measurements by Pulsed ESR. *J. Magn. Reson.* **2018**, *286*, 163−171.

https://dx.doi.org/10.1021/acs.jpcb.0c00739
J. Phys. Chem. B 2020, 124, 2788−2797

(40) Wort, J. L.; Ackermann, K.; Giannoulis, A.; Stewart, A. J.; Norman, D. G.; Bode, B. E. Sub-Micromolar Pulse Dipolar EPR Spectroscopy Reveals Increasing Cu ^{II} -labelling of Double-Histidine Motifs with Lower Temperature. *Angew. Chem.* **2019**, *131*, 11807−11811.
(41) Sameach, H.; Ghosh, S.; Gevorkyan-Airapetov, L.; Saxena, S.; Ruthstein, S. EPR Spectroscopy Detects Various Active State Conformations of the Transcriptional Regulator CueR. *Angew. Chem., Int. Ed.* **2019**, *58*, 3053−3056.
(42) Lawless, M. J.; Pettersson, J. R.; Rule, G. S.; Lanni, F.; Saxena, S. ESR Resolves the C Terminus Structure of the Ligand-Free Human Glutathione S-Transferase A1-1. *Biophys. J.* **2018**, *114*, 592−601.
(43) Gamble Jarvi, A.; Cunningham, T. F.; Saxena, S. Efficient Localization of a Native Metal Ion within a Protein by Cu $^{2+}$ -Based EPR Distance Measurements. *Phys. Chem. Chem. Phys.* **2019**, *21*, 10238−10243.
(44) Gamble Jarvi, A.; Ranguelova, K.; Ghosh, S.; Weber, R. T.; Saxena, S. On the Use of Q-Band Double Electron−Electron Resonance To Resolve the Relative Orientations of Two Double Histidine-Bound Cu $^{2+}$ Ions in a Protein. *J. Phys. Chem. B* **2018**, *122*, 10669−10677.
(45) Ghosh, S.; Saxena, S.; Jeschke, G. Rotamer Modelling of Cu(II) Spin Labels Based on the Double-Histidine Motif. *Appl. Magn. Reson.* **2018**, *49*, 1281−1298.
(46) Ding, F.; Layten, M.; Simmerling, C. Solution Structure of HIV-1 Protease Flaps Probed by Comparison of Molecular Dynamics Simulation Ensembles and EPR Experiments. *J. Am. Chem. Soc.* **2008**, *130*, 7184−7185.
(47) Bhatnagar, J.; Freed, J. H.; Crane, B. R. Rigid Body Refinement of Protein Complexes with Long-Range Distance Restraints from Pulsed Dipolar ESR. *Methods Enzymol.* **2007**, *423*, 117−133.
(48) Kazmier, K.; Alexander, N. S.; Meiler, J.; Mchaourab, H. S. Algorithm for Selection of Optimized EPR Distance Restraints for de Novo Protein Structure Determination. *J. Struct. Biol.* **2011**, *173*, 549−557.
(49) Polyhach, Y.; Godt, A.; Bauer, C.; Jeschke, G. Spin Pair Geometry Revealed by High-Field DEER in the Presence of Conformational Distributions. *J. Magn. Reson.* **2007**, *185*, 118−129.
(50) Sale, K.; Song, L.; Liu, Y.-S.; Perozo, E.; Fajer, P. Explicit Treatment of Spin Labels in Modeling of Distance Constraints from Dipolar EPR and DEER. *J. Am. Chem. Soc.* **2005**, *127*, 9334−9335.
(51) Boura, E.; Rózycki, B.; Herrick, D. Z.; Chung, H. S.; Vecer, J.; Eaton, W. A.; Cafiso, D. S.; Hummer, G.; Hurley, J. H. Solution Structure of the ESCRT-I Complex by Small-Angle X-Ray Scattering, EPR, and FRET Spectroscopy. *Proc. Natl. Acad. Sci. U.S.A.* **2011**, *108*, 9437−9442.
(52) Hirst, S. J.; Alexander, N.; Mchaourab, H. S.; Meiler, J. RosettaEPR: An Integrated Tool for Protein Structure Determination from Sparse EPR Data. *J. Struct. Biol.* **2011**, *173*, 506−514.
(53) Tikhonova, I. G.; Best, R. B.; Engel, S.; Gershengorn, M. C.; Hummer, G.; Costanzi, S. Atomistic Insights into Rhodopsin Activation from a Dynamic Model. *J. Am. Chem. Soc.* **2008**, *130*, 10141−10149.
(54) Galiano, L.; Ding, F.; Veloro, A. M.; Blackburn, M. E.; Simmerling, C.; Fanucci, G. E. Drug Pressure Selected Mutations in HIV-1 Protease Alter Flap Conformations. *J. Am. Chem. Soc.* **2009**, *131*, 430−431.
(55) Jao, C. C.; Hegde, B. G.; Chen, J.; Haworth, I. S.; Langen, R. Structure of Membrane-Bound -Synuclein from Site-Directed Spin Labeling and Computational Refinement. *Proc. Natl. Acad. Sci. U.S.A.* **2008**, *105*, 19666−19671.
(56) Islam, S. M.; Stein, R. A.; Mchaourab, H. S.; Roux, B. Structural Refinement from Restrained-Ensemble Simulations Based on EPR/DEER Data: Application to T4 Lysozyme. *J. Phys. Chem. B* **2013**, *117*, 4740−4754.
(57) Case, D.; Ben-Shalom, I.; Brozell, S.; Cerutti, D.; Cheatham, T., III; Cruzeiro, V.; Darden, T.; Duke, R.; Ghoreishi, D.; Gilson, M.; et al. *AMBER 2018*; University of California: San Francisco, 2018.
(58) *The PyMOL Molecular Graphics System*, version 1.8; Schrödinger, LLC, 2015.
(59) Maier, J. A.; Martinez, C.; Kasavajhala, K.; Wickstrom, L.; Hauser, K. E.; Simmerling, C. Ff14SB: Improving the Accuracy of Protein Side Chain and Backbone Parameters from Ff99SB. *J. Chem. Theory Comput.* **2015**, *11*, 3696−3713.
(60) Wang, J.; Wolf, R. M.; Caldwell, J. W.; Kollman, P. A.; Case, D. A. Development and Testing of a General Amber Force Field. *J. Comput. Chem.* **2004**, *25*, 1157−1174.
(61) Moses, V.; Tastan Bishop, Ö.; Lobb, K. A. The Evaluation and Validation of Copper (II) Force Field Parameters of the Auxiliary Activity Family 9 Enzymes. *Chem. Phys. Lett.* **2017**, *678*, 91−97.
(62) Op't Hol, B. T.; Merz, K. M. Insights into Cu(I) Exchange in HAH1 Using Quantum Mechanical and Molecular Simulations. *Biochemistry* **2007**, *46*, 8816−8826.
(63) Zhu, Y.; Su, Y.; Li, X.; Wang, Y.; Chen, G. Evaluation of Amber Force Field Parameters for Copper(II) with Pyridylmethyl-Amine and Benzimidazolylmethyl-Amine Ligands: A Quantum Chemical Study. *Chem. Phys. Lett.* **2008**, *455*, 354−360.
(64) Cieplak, P.; Cornell, W. D.; Bayly, C.; Kollman, P. A. Application of the Multimolecule and Multiconformational RESP Methodology to Biopolymers: Charge Derivation for DNA, RNA, and Proteins. *J. Comput. Chem.* **1995**, *16*, 1357−1377.
(65) Frisch, M. J.; Trucks, G. W.; Schlegel, H. B.; Scuseria, G. E.; Robb, M. A.; Cheeseman, J. R.; Scalmani, G.; Barone, V.; Petersson, G. A.; Nakatsuji, H.; et al. *Gaussian 16*, revision C.01; Gaussian, Inc.: Wallingford, CT, 2016.
(66) Wang, J.; Wang, W.; Kollman, P. A.; Case, D. A. Automatic Atom Type and Bond Type Perception in Molecular Mechanical Calculations. *J. Mol. Graph. Model.* **2006**, *25*, 247−260.
(67) Peters, M. B.; Yang, Y.; Wang, B.; Füsti-Molnár, L.; Weaver, M. N.; Merz, K. M. Structural Survey of Zinc-Containing Proteins and Development of the Zinc AMBER Force Field (ZAFF). *J. Chem. Theory Comput.* **2010**, *6*, 2935−2947.
(68) Jorgensen, W. L.; Chandrasekhar, J.; Madura, J. D.; Impey, R. W.; Klein, M. L. Comparison of Simple Potential Functions for Simulating Liquid Water. *J. Chem. Phys.* **1983**, *79*, 926−935.
(69) Berendsen, H. J. C.; Postma, J. P. M.; van Gunsteren, W. F.; DiNola, A.; Haak, J. R. Molecular Dynamics with Coupling to an External Bath. *J. Chem. Phys.* **1984**, *81*, 3684−3690.
(70) Jeschke, G.; Chechik, V.; Ionita, P.; Godt, A.; Zimmermann, H.; Banham, J.; Timmel, C. R.; Hilger, D.; Jung, H. DeerAnalysis2006—a Comprehensive Software Package for Analyzing Pulsed ELDOR Data. *Appl. Magn. Reson.* **2006**, *30*, 473−498.
(71) Brandi-Blanco, M. P.; de Benavides-Giménez, M. M.; González-Pérez, J. M.; Choquesillo-Lazarte, D. *Cis*-[*N* -(4-Chlorobenzyl)-Iminodiacetato-κ^3 N, O, O′]Bis(1*H* -Imidazole-κ N^3)Copper(II). *Acta Crystallogr., Sect. E: Struct. Rep. Online* **2007**, *63*, m1678−m1679.
(72) Fee, J. A. Copper Proteins Systems Containing the "Blue" Copper Center. In *Biochemistry*; Fee, J. A.; Dunn, M. F.; Schneider, W.; Orchin, M.; Bollinger, D. M., Eds.; Springer: Berlin, Heidelberg, 1975; pp 1−60.
(73) Burns, C. J.; Field, L. D.; Hambley, T. W.; Lin, T.; Ridley, D. D.; Turner, P.; Wilkinson, M. P. X-Ray Crystal Structural Determination of Copper (II)-Nitrilotriacetic Acid-Bis (N-Methyl-imidazol-2-Yl) Ketone Ternary Complex. *ARKIVOC* **2001**, *7*, 157−165.
(74) Hawkins, G. D.; Cramer, C. J.; Truhlar, D. G. Parametrized Models of Aqueous Free Energies of Solvation Based on Pairwise Descreening of Solute Atomic Charges from a Dielectric Medium. *J. Phys. Chem. A* **1996**, *100*, 19824−19839.
(75) Gronenborn, A.; Filpula, D.; Essig, N.; Achari, A.; Whitlow, M.; Wingfield, P.; Clore, G. A Novel, Highly Stable Fold of the Immunoglobulin Binding Domain of Streptococcal Protein G. *Science* **1991**, *253*, 657−661.
(76) Alexander, P.; Fahnestock, S.; Lee, T.; Orban, J.; Bryan, P. Thermodynamic Analysis of the Folding of the Streptococcal Protein G IgG-Binding Domains B1 and B2: Why Small Proteins Tend to

https://dx.doi.org/10.1021/acs.jpcb.0c00739
J. Phys. Chem. B 2020, 124, 2788−2797

Have High Denaturation Temperatures. *Biochemistry* **1992**, *31*, 3597−3603.
(77) Dockter, C.; Volkov, A.; Bauer, C.; Polyhach, Y.; Joly-Lopez, Z.; Jeschke, G.; Paulsen, H. Refolding of the Integral Membrane Protein Light-Harvesting Complex II Monitored by Pulse EPR. *Proc. Natl. Acad. Sci. U.S.A.* **2009**, *106*, 18485−18490.
(78) Walsh, J. D.; Meier, K.; Ishima, R.; Gronenborn, A. M. NMR Studies on Domain Diffusion and Alignment in Modular GB1 Repeats. *Biophys. J.* **2010**, *99*, 2636−2646.
(79) Sengupta, I.; Nadaud, P. S.; Helmus, J. J.; Schwieters, C. D.; Jaroniec, C. P. Protein Fold Determined by Paramagnetic Magic-Angle Spinning Solid-State NMR Spectroscopy. *Nat. Chem.* **2012**, *4*, 410−417.
(80) Nadaud, P. S.; Helmus, J. J.; Kall, S. L.; Jaroniec, C. P. Paramagnetic Ions Enable Tuning of Nuclear Relaxation Rates and Provide Long-Range Structural Restraints in Solid-State NMR of Proteins. *J. Am. Chem. Soc.* **2009**, *131*, 8108−8120.
(81) Thoms, S.; Max, K. E. A.; Wunderlich, M.; Jacso, T.; Lilie, H.; Reif, B.; Heinemann, U.; Schmid, F. X. Dimer Formation of a Stabilized Gβ1 Variant: A Structural and Energetic Analysis. *J. Mol. Biol.* **2009**, *391*, 918−932.
(82) Lindman, S.; Xue, W.-F.; Szczepankiewicz, O.; Bauer, M. C.; Nilsson, H.; Linse, S. Salting the Charged Surface: PH and Salt Dependence of Protein G B1 Stability. *Biophys. J.* **2006**, *90*, 2911−2921.
(83) Muñoz, V.; Thompson, P. A.; Hofrichter, J.; Eaton, W. A. Folding Dynamics and Mechanism of β-Hairpin Formation. *Nature* **1997**, *390*, 196−199.
(84) Morrone, A.; Giri, R.; Toofanny, R. D.; Travaglini-Allocatelli, C.; Brunori, M.; Daggett, V.; Gianni, S. GB1 Is Not a Two-State Folder: Identification and Characterization of an On-Pathway Intermediate. *Biophys. J.* **2011**, *101*, 2053−2060.
(85) Bauer, M.; Xue, W.-F.; Linse, S. Protein GB1 Folding and Assembly from Structural Elements. *Int. J. Mol. Sci.* **2009**, *10*, 1552−1566.
(86) Engelhard, D. M.; Meyer, A.; Berndhäuser, A.; Schiemann, O.; Clever, G. H. Di-Copper(II) DNA G-Quadruplexes as EPR Distance Rulers. *Chem. Commun.* **2018**, *54*, 7455−7458.
(87) Denysenkov, V. P.; Prisner, T. F.; Stubbe, J.; Bennati, M. High-Field Pulsed Electron-Electron Double Resonance Spectroscopy to Determine the Orientation of the Tyrosyl Radicals in Ribonucleotide Reductase. *Proc. Natl. Acad. Sci. U.S.A.* **2006**, *103*, 13386−13390.
(88) Schiemann, O.; Cekan, P.; Margraf, D.; Prisner, T. F.; Sigurdsson, S. T. Relative Orientation of Rigid Nitroxides by PELDOR: Beyond Distance Measurements in Nucleic Acids. *Angew. Chem., Int. Ed.* **2009**, *48*, 3292−3295.
(89) Yang, Z.; Kise, D.; Saxena, S. An Approach towards the Measurement of Nanometer Range Distances Based on Cu^{2+} Ions and ESR. *J. Phys. Chem. B* **2010**, *114*, 6165−6174.
(90) Yang, Z.; Ji, M.; Saxena, S. Practical Aspects of Copper Ion-Based Double Electron Electron Resonance Distance Measurements. *Appl. Magn. Reson.* **2010**, *39*, 487−500.
(91) Bowen, A. M.; Jones, M. W.; Lovett, J. E.; Gaule, T. G.; McPherson, M. J.; Dilworth, J. R.; Timmel, C. R.; Harmer, J. R. Exploiting Orientation-Selective DEER: Determining Molecular Structure in Systems Containing Cu(II) Centres. *Phys. Chem. Chem. Phys.* **2016**, *18*, 5981−5994.
(92) Abé, C.; Klose, D.; Dietrich, F.; Ziegler, W. H.; Polyhach, Y.; Jeschke, G.; Steinhoff, H.-J. Orientation Selective DEER Measurements on Vinculin Tail at X-Band Frequencies Reveal Spin Label Orientations. *J. Magn. Reson.* **2012**, *216*, 53−61.
(93) Bode, B. E.; Plackmeyer, J.; Prisner, T. F.; Schiemann, O. PELDOR Measurements on a Nitroxide-Labeled Cu(II) Porphyrin: Orientation Selection, Spin-Density Distribution, and Conformational Flexibility. *J. Phys. Chem. A* **2008**, *112*, 5064−5073.
(94) Sarver, J.; Silva, K. I.; Saxena, S. Measuring Cu^{2+}-Nitroxide Distances Using Double Electron−Electron Resonance and Saturation Recovery. *Appl. Magn. Reson.* **2013**, *44*, 583−594.
(95) Breitgoff, F. D.; Keller, K.; Qi, M.; Klose, D.; Yulikov, M.; Godt, A.; Jeschke, G. UWB DEER and RIDME Distance Measurements in Cu(II)−Cu(II) Spin Pairs. *J. Magn. Reson.* **2019**, *308*, No. 106560.
(96) Marko, A.; Prisner, T. F. An Algorithm to Analyze PELDOR Data of Rigid Spin Label Pairs. *Phys. Chem. Chem. Phys.* **2013**, *15*, 619−627.
(97) Marko, A.; Margraf, D.; Cekan, P.; Sigurdsson, S. T.; Schiemann, O.; Prisner, T. F. Analytical Method to Determine the Orientation of Rigid Spin Labels in DNA. *Phys. Rev. E* **2010**, *81*, No. 021911.
(98) Lovett, J. E.; Bowen, A. M.; Timmel, C. R.; Jones, M. W.; Dilworth, J. R.; Caprotti, D.; Bell, S. G.; Wong, L. L.; Harmer, J. Structural Information from Orientationally Selective DEER Spectroscopy. *Phys. Chem. Chem. Phys.* **2009**, *11*, 6840.
(99) Tkach, I.; Pornsuwan, S.; Höbartner, C.; Wachowius, F.; Sigurdsson, S. Th.; Baranova, T. Y.; Diederichsen, U.; Sicoli, G.; Bennati, M. Orientation Selection in Distance Measurements between Nitroxide Spin Labels at 94 GHz EPR with Variable Dual Frequency Irradiation. *Phys. Chem. Chem. Phys.* **2013**, *15*, 3433.

https://dx.doi.org/10.1021/acs.jpcb.0c00739
J. Phys. Chem. B 2020, 124, 2788−2797